

Strain-field effects on the formation and migration energies of self interstitials in α -Fe from first principles

Zhengzheng Chen,¹ Nicholas Kioussis,¹ Nasr Ghoniem,² and Dariush Seif²¹*Department of Physics, California State University, Northridge, California 91330-8268, USA*²*Department of Mechanical and Aerospace Engineering, University of California, Los Angeles, California 90095-1597, USA*

(Received 15 September 2009; revised manuscript received 5 February 2010; published 5 March 2010)

Ab initio electronic structure calculations are employed to study the stability and mobility of mono-self interstitial atoms (SIA) in α -Fe under external deformation. The *ab initio* results indicate that the volumetric and uniaxial strain dependences of the SIA formation energy are different in the expansion and compression regimes, in contrast to the linear behavior in continuum elasticity theory. We find a $\langle 111 \rangle \rightarrow \langle 100 \rangle$ SIA reorientation mechanism induced by uniaxial expansion which proceeds via $\langle 11x \rangle|_{x=2.7}$ configuration. Volumetric and uniaxial deformations are also found to have a considerable influence on the migration paths and activation energy barriers for the $\langle 110 \rangle \{110\} \leftrightarrow \langle 100 \rangle \{100\}$ transformation and the $\langle 111 \rangle \leftrightarrow \langle 100 \rangle$ reorientation. The results reveal that (i) the volumetric expansion (compression) decreases (increases) substantially the migration energy barrier and renders the diffusion process three (one) dimensional, (ii) the uniaxial strain removes (decreases) the migration energy barrier for the $\langle 111 \rangle \rightarrow \langle 11x \rangle|_{x=2.7} (\langle 11x \rangle|_{x=2.7} \rightarrow \langle 100 \rangle)$ transformation, leading to spontaneous reorientation of the $\langle 111 \rangle$ SIA, and (iii) the uniaxial deformation breaks the cubic symmetry of the system and in turn induces anisotropy of the migration rates along different directions. These calculations demonstrate that changes in the electronic structure induced by global elastic deformation lead to additional contributions to the formation and migration energies, which cannot be adequately accounted for neither by elasticity theory nor by empirical interatomic potentials.

DOI: [10.1103/PhysRevB.81.094102](https://doi.org/10.1103/PhysRevB.81.094102)

PACS number(s): 61.82.Bg, 71.15.Mb, 73.20.-r

I. INTRODUCTION

Ferritic, martensitic steels are proposed as structural materials in many applications in fission and fusion energy systems. Understanding the physics of radiation interaction with iron is fundamental to the development of advanced structural steels in such applications. Many irradiation effects, including irradiation embrittlement and long-term aging of cascades, are mediated by the formation, transport, and annihilation of self interstitial atom (SIA) clusters.¹ Although relatively rare in metals under normal conditions, transmission electron microscopy (TEM) measurements have demonstrated the nucleation of SIA clusters in the early stage of displacement cascades, when the irradiation dose increases above ~ 1 dpa.²⁻⁴ Thus, understanding the stability and mobility of SIA clusters in the severe irradiation conditions found in these environments is important in improving the in-service performance of reactor pressure vessel (RPV) steels.

Given their crucial role, intensive studies have focused during the past decade on determining the formation and migration energies of SIAs in macroscopically undeformed α -Fe crystals from density-functional theory (DFT) calculations⁵⁻⁷ and atomistic simulations employing empirical potentials.⁸⁻¹¹ For the single SIA in α -Fe, both experiments¹² and DFT calculations^{5,6} agree that the $\langle 110 \rangle$ dumbbell is the ground-state configuration, which is 0.7 eV below the $\langle 111 \rangle$ dumbbell. These results are in contrast with those from two empirical potentials using the Finnis-Sinclair¹³ type and modified embedded atom method (MEAM)¹⁴ type. Upon increasing the size of SIA clusters, atomistic simulations have shown that there is a transition of the ground-state configuration from the $\langle 110 \rangle$ to the $\langle 111 \rangle$

dumbbells.^{7,11,15} In addition, Fu *et al.* studied the migration paths and corresponding energy barriers of a single SIA in α -Fe and identified the three-dimensional migration mechanism responsible for the unusually large barrier of 0.34 eV.⁶

On the other hand, the properties of SIAs in α -Fe in the severe conditions of irradiation, where the solid undergoes deformations under applied loads (volumetric, uniaxial, etc.) have not been fully explored. Recently, Gavini investigated the effect of macroscopic deformations on the energetics of vacancies in aluminum.¹⁶ Molecular dynamics simulations of oversized substitutional Cu atoms in α -Fe have shown that the dilational strain in the surrounding Fe lattice leads to the reorientation of single SIA.¹⁷ Interestingly, recent *in situ* TEM experiments in high-energy electron irradiated α -Fe have observed a *spontaneous* reorientation of SIA clusters from the $\langle 111 \rangle$ to the $\langle 100 \rangle$ configuration.¹⁸ It was suggested that the underlying mechanism is the interaction of the SIA with the strain field of nearby dislocations. This is in contrast with the reaction mechanism found in the molecular-dynamics simulations of Marian *et al.*¹⁹ involving the coalescence of the mobile $\frac{1}{2}[111]$ and $\frac{1}{2}[\bar{1}\bar{1}\bar{1}]$ loops: $\frac{1}{2}[111] + \frac{1}{2}[\bar{1}\bar{1}\bar{1}] \rightarrow [100]$. These results raise the interesting question on the effect of the external deformation on the stability and mobility of SIAs in α -Fe.

Anisotropic diffusion of defects in strained crystals has received considerable attention during the past few decades, mainly motivated by a variety of applications in the radiation damage field²⁰⁻²³ and in the semiconductor field.^{24,25} These efforts benefited from established continuum methods of anisotropic diffusion,²⁶ culminating in a comprehensive formulation of the connection between atomistic equations of motion and continuum diffusion by Dederichs and Schroeder.²⁷ These studies demonstrated that the interaction energy at the

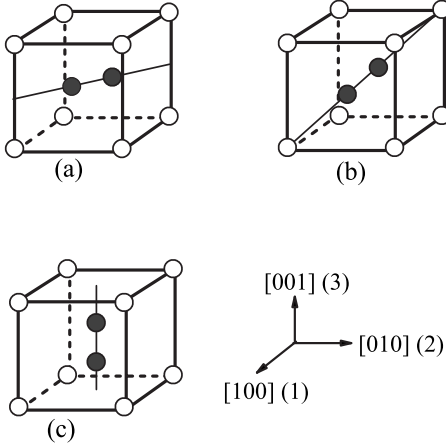


FIG. 1. Schematic representation of the (a) $\langle 110 \rangle$, (b) $\langle 111 \rangle$, and (c) $\langle 100 \rangle$ SIA configurations and the crystallographic coordinate system.

saddle point leads to an anisotropic diffusion tensor, even for cubic crystals with isotropic defects, such as vacancies.²⁷ Current progress in electronic structure calculations are allowing greater insight into the physical origins of defect properties in crystalline solids and as such, it is of interest to elucidate the origins of diffusion anisotropy of SIAs in strained crystals.

The objective of this work is to utilize *ab initio* electronic structure calculations to study the influence of volumetric and uniaxial external deformation on the stability, mobility, and migration paths of self interstitial atoms in α -Fe. The paper is organized as follows. In Sec. II, we briefly summarize the methodology. The results for the formation energies and migration energy barriers of different SIA configurations under the two types of external deformation are presented in Sec. III and the underlying mechanisms are discussed. Finally, a brief summary is given in Sec. IV.

II. METHODOLOGY

Spin-polarized DFT calculations were performed with the Vienna *ab initio* simulation package (VASP) (Refs. 28 and 29) using the Perdew-Burke-Enzerhof generalized gradient approximation (GGA) (Ref. 30) for the exchange and correlation functionals. The electron-ion interactions were treated within the projected augmented wave (PAW) approach.³¹ An energy cutoff of 300 eV was used for the plane-wave expansion of the wave functions. We have employed a 129-atom $4 \times 4 \times 4$ supercell containing an interstitial atom to form a mono SIA and a $4 \times 4 \times 4$ k -point mesh according to the Monkhorst-Pack scheme.³² Methfessel-Paxton broadening scheme is used for Brillouin-zone integration with smear width as 0.10 eV. These settings yield an energy convergence of less than 3 meV/atom. All atoms were fully relaxed until the maximum force is smaller than 0.03 eV/Å. The three SIAs considered in this study are the $\langle 110 \rangle$, $\langle 111 \rangle$, and $\langle 100 \rangle$ configurations, respectively, shown in Fig. 1. We have studied both isotropic volumetric and uniaxial types of deformation. In the former case, the strain tensor is represented as³³

$\varepsilon_{11} = \varepsilon_{22} = \varepsilon_{33} = \varepsilon$ and $\varepsilon_{12} = \varepsilon_{13} = \varepsilon_{23} = 0$, corresponding to the volumetric strain of $\varepsilon_v = 3\varepsilon$. In the latter case, $\varepsilon_{11} = \varepsilon$, while all other components vanish. Thus, the effect of uniaxial strain on the $\langle 110 \rangle$ and $\langle 100 \rangle$ configurations can be determined.

In the case of volumetric deformation, the formation energy of the SIAs at constant volume is given by³⁴

$$E_{\text{SIA}}^f(V) = E\left(N+1; \frac{N+1}{N}V\right) - \frac{N+1}{N}E(N;V), \quad (1)$$

where $E(N+1; \frac{N+1}{N}V)$ and $E(N;V)$ are the total energies of the system, with $N+1$ atoms in the renormalized volume $\frac{N+1}{N}V$ and that of the perfect bulk with N atoms in volume V , respectively. This definition satisfies the conservation of both number of atoms and volume in the initial and final states.

In the case of uniaxial deformation, on the other hand, the volume renormalization cannot be used because this deformation is anisotropic. Without taking the “pressure correction” (Ref. 5) into account, $E_{\text{SIA}}^f(\varepsilon_{ij})$ is given by^{16,35}

$$E_{\text{SIA}}^f(\varepsilon_{ij}) = E(N+1; \varepsilon_{ij}) - \frac{N+1}{N}E(N; \varepsilon_{ij}), \quad (2)$$

where $E(N+1; \varepsilon_{ij})$ and $E(N; \varepsilon_{ij})$ are the total energies of the supercell containing N atoms with and without a SIA under the deformation mode with strain tensor ε_{ij} , respectively.

In the present work, we have also tried to bridge the results of the *ab initio* calculations with those of atomistic simulations using empirical potentials and with those employing continuum elasticity theory. In the latter case, the elastic multipole representation of defects (EMRDs) method was employed to describe the interaction between the SIA and the external strain field. The interaction energy E_{int} can be expressed as^{27,36}

$$E_{\text{int}} = - \sum_{i,j=1}^3 P_{ij}^{(1)} \varepsilon_{ij}, \quad (3)$$

where ε_{ij} are the external strain matrix elements and $\mathbf{P}^{(1)}$ is the dipole tensor induced by an SIA which can be in turn obtained from the atomistic displacement field $\mathbf{u}(\mathbf{x})$. Following the method of Siems and Teodosiu, the component of $\mathbf{u}(\mathbf{x})$ along the i th direction, $u_i(\mathbf{x})$, is^{36,37}

$$u_i(\mathbf{x}) = \sum_{k=1}^{\infty} \frac{(-1)^k}{k!} G_{ij,q_1 \dots q_k}(\mathbf{x}) P_{q_1 \dots q_k}^{(k)}, \quad (4)$$

where $\mathbf{G}(\mathbf{x})$ is the elastic Green’s function tensor of the material and $\mathbf{P}^{(k)}$ are the multipolar moment tensors. The multipolar moment tensors corresponding to $k=1, 2$, and 3 are the dipole, quadrupole, and octupole moments, respectively. In the present work, we have used the *isotropic* elastic Green’s functions for simplicity and considered Eq. (4) to the lowest order, keeping only the dipole tensor $\mathbf{P}^{(1)}$. The displacement field $u_i(\mathbf{x}_j)$ was determined by optimized atomistic simulations and the linear least-squares problem of Eq. (4) was solved to determine $\mathbf{P}^{(1)}$.

TABLE I. *Ab initio* values of formation energies, E_{SIA}^f of different SIA configurations at equilibrium. For comparison, we also list the corresponding values of previous DFT calculations.

	$E_{\text{SIA}}^f(\varepsilon=0)$		
	$\langle 110 \rangle$	$\langle 111 \rangle$	$\langle 100 \rangle$
This work	3.86	4.56	4.96
SIESTA 129 atoms ^a	3.64	4.34	4.64
VASP 55 atoms ^b	3.96	4.75	5.07
VASP 129 atoms ^b	3.94	4.66	5.04

^aReference 6.

^bReference 5.

III. RESULTS

A. *Ab initio* energetics of SIAs

In Table I, we list the *ab initio* calculated formation energies, E_{SIA}^f , of the three SIA configurations at equilibrium, where all $\varepsilon_{ij}=0$, and compare them to previous DFT calculations.^{5,6} The lowest-energy configuration is the $\langle 110 \rangle$ dumbbell in agreement with experiments.¹² The $\langle 111 \rangle$ and $\langle 100 \rangle$ SIA configurations are 0.7 and 1.1 eV higher in energy relative to that of the $\langle 110 \rangle$ dumbbell, respectively, in agreement with previous DFT calculations.^{5,6}

Figure 2(a) displays the *ab initio* calculated E_{SIA}^f of the three SIA configurations as a function of volumetric strain, ε_v . It is clear that the volumetric deformation has a significant influence on E_{SIA}^f , which monotonically decreases (increases) with increasing volumetric expansion (compression) corresponding to $\varepsilon_v > 0$ ($\varepsilon_v < 0$) strain. This suggests that nucleation of these SIAs is favorable under expansion as opposed to compression. For example, E_{SIA}^f decreases by about 2.2 eV upon expansion of the supercell volume from $0.9V_0$ to $1.1V_0$, where V_0 is the equilibrium volume. The volumetric strain behavior of E_{SIA}^f is independent of the SIA's orientation and its origin lies in the interaction between the dilational strain produced by the SIA and the external deformation. Thus, the release (accumulation) of elastic energy under volumetric expansion (compression) results in the reduction (increase) of E_{SIA}^f .

Figures 2(b) and 2(c) show the *ab initio* calculated E_{SIA}^f for the three SIA configurations as a function of uniaxial strain ε_{11} (ε_{22}) and ε_{33} , respectively. The results clearly show that $\langle 111 \rangle$ SIA is insensitive to the uniaxial strain direction, which can be attributed to its orientational symmetry with respect to the loading axis. The three cubic axes have the same orientation with respect to $\langle 111 \rangle$. In contrast, $E_{\langle 110 \rangle}^f$ and $E_{\langle 100 \rangle}^f$ depend on the orientation of the loading axis. As shown in Fig. 2(b), $E_{\langle 110 \rangle}^f$ and $E_{\langle 100 \rangle}^f$ decrease when ε_{11} (ε_{22}) < 0 and almost do not change when ε_{11} (ε_{22}) > 0 . $E_{\langle 111 \rangle}^f - E_{\langle 100 \rangle}^f$ decreases to 0.21 eV under ε_{11} (ε_{22}) = -3% and increases to 0.67 eV under ε_{11} (ε_{22}) = 3%, respectively. Under ε_{33} [shown in Fig. 2(c)], $E_{\langle 100 \rangle}^f$ decreases monotonically under uniaxial strains, similar to the effect of volumetric deformation. $E_{\langle 110 \rangle}^f$ behavior is similar to $E_{\langle 100 \rangle}^f$ except that the formation energy is very insensitive to compression. In contrast to the case of ε_{11} (ε_{22}), $E_{\langle 111 \rangle}^f - E_{\langle 100 \rangle}^f$ decreases

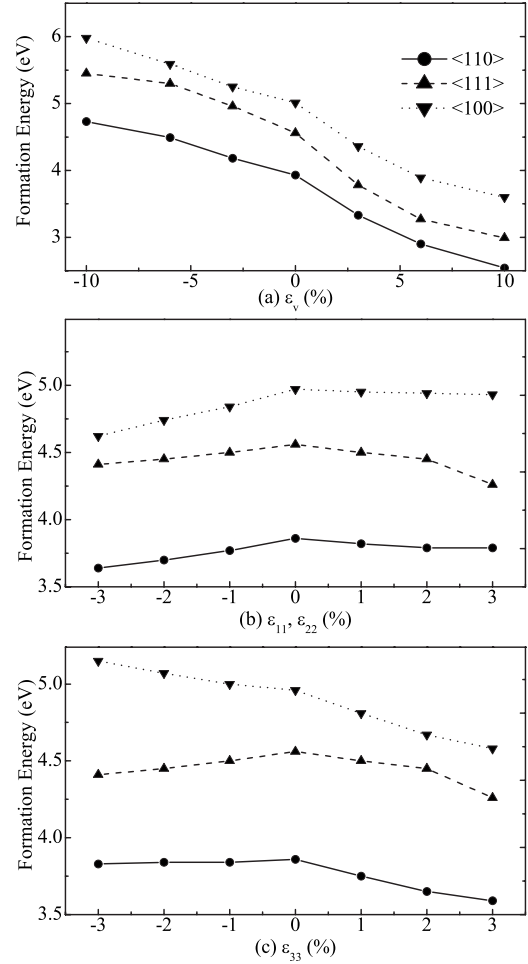


FIG. 2. Formation energies of the $\langle 110 \rangle$, $\langle 111 \rangle$, and $\langle 100 \rangle$ SIA configurations as a function of (a) isotropic volumetric, (b) uniaxial strain ε_{11} (ε_{22}), and (c) uniaxial strain ε_{33} .

to 0.22 eV under $\varepsilon_{33}=2\%$ and increases to 0.74 eV under $\varepsilon_{33}=-3\%$, respectively. Comparing Figs. 2(a) and 2(b), one should note that $E_{\langle 110 \rangle}^f(\pm\varepsilon_{11}) \approx E_{\langle 110 \rangle}^f(\mp\varepsilon_{33})$ and also $E_{\langle 100 \rangle}^f(\pm\varepsilon_{11}) \approx E_{\langle 100 \rangle}^f(\mp\varepsilon_{33})$, with ε_{11} and $\varepsilon_{33} < 0$. This feature indicates that the lateral relaxation (perpendicular and opposite to the external deformation) of the system has an effect on the E_{SIA}^f which cannot be ignored. Clearly, the deformation plays an important role on the formation energies of SIAs with different orientations.

Within the elastic continuum formalism of anisotropic diffusion of particles (defects) in an elastically deformed crystal,^{20,21,27} the equilibrium population of defects under an applied strain field depends only on the defect energy at its equilibrium position and not on the saddle-point energy.²⁷ Aziz³⁸ and Daw *et al.*³⁹ pointed out that $E_{\text{SIA}}^f(\boldsymbol{\sigma})$ in the presence of an external stress must include the stress-strain work required to distort the system against the applied stress field and can be written as

$$E_{\text{SIA}}^f(\boldsymbol{\sigma}) = E_{\text{SIA}}^f(0) + \boldsymbol{\sigma} : \mathbf{V}^f. \quad (5)$$

Here, \mathbf{V}^f is the formation volume tensor and $\boldsymbol{\sigma}$ is the entire stress tensor. Using the *ab initio* calculated values of $E_{\text{SIA}}^f(\boldsymbol{\sigma})$

TABLE II. Strain-dependent diagonal matrix elements of the formation volume, V_{11}^f (or V_{22}^f) and V_{33}^f , normalized to the zero-strain volume, $\Omega_0=11.43 \text{ \AA}^3$, of α -Fe under uniaxial strain $\varepsilon_{ii}|_{i=1,2,3} = \pm 3\%$ for the $\langle 110 \rangle$, $\langle 111 \rangle$, and $\langle 100 \rangle$ SIA configurations.

	V_{11}^f/Ω_0		V_{33}^f/Ω_0	
	$\varepsilon_{11}=-3\%$	$\varepsilon_{11}=3\%$	$\varepsilon_{33}=-3\%$	$\varepsilon_{33}=3\%$
$\langle 110 \rangle$	-0.42	0.13	-0.08	0.52
$\langle 111 \rangle$	-0.29	0.58	-0.29	0.58
$\langle 100 \rangle$	-0.67	0.08	0.35	0.75

[Figs. 2(b) and 2(c)] under uniaxial deformation, where the stress tensor reduces to

$$\sigma_{11}(\sigma_{22}, \sigma_{33}) = -C_{11}\varepsilon_{11}(\varepsilon_{22}, \varepsilon_{33}), \quad (6)$$

with $C_{11}=243 \text{ GPa}$, we have calculated the diagonal matrix elements V_{ii}^f from Eq. (5). The off-diagonal elements require shear deformation which are not investigated in the present work. Values of V_{11}^f (V_{22}^f) under a uniaxial strain of $\varepsilon_{11}(\varepsilon_{22}) = \pm 3\%$ and V_{33}^f under $\varepsilon_{33} = \pm 3\%$ are listed in Table II for the three SIA configurations. These results clearly demonstrate that the formation volume tensor is anisotropic and is a function of external deformation due to the fact that the *ab initio* calculated formation energy (Fig. 2) is anisotropic and depends nonlinearly on applied stress. In sharp contrast, the predictions of linear elasticity,³⁸ to be discussed in Sec. III B, give a formation volume tensor independent of stress because $E_{\text{SIA}}^f(\boldsymbol{\sigma})$ varies linearly with applied stress for all three SIA configurations.

For the volumetric deformation, we have also calculated the formation enthalpy H_{SIA}^f under constant pressure p (Ref. 40)

$$H_{\text{SIA}}^f(p) = E_{\text{SIA}}^f(p) + p\Delta V = E(N+1;p) - \frac{N+1}{N}E(N;p) + p\Delta V, \quad (7)$$

where $E(N+1;p)$ and $E(N;p)$ are the total energies of the system with and without the SIA under the same pressure p , respectively, and the SIA formation volume, ΔV , represents the change in volume from the N -atom bulk to the $(N+1)$ -atom system under p given by^{40,41}

$$\Delta V = V(N+1;p) - \frac{N+1}{N}V(N;p). \quad (8)$$

The energies $E(N+1;p) = E[N+1; V_p(N+1)]$ and $E(N;p) = E[N; V_p(N)]$, where $V_p(N)$ and $V_p(N+1)$ are the volumes for the N - and $(N+1)$ -atom systems corresponding to the same pressure $p = -\frac{dE(N,V)}{dV}|_{V_p(N)} = -\frac{dE(N+1,V)}{dV}|_{V_p(N+1)}$. The calculated bulk modulus $B=179 \text{ GPa}$ is in good agreement with the experimental value⁴² of 168 GPa .

The formation enthalpies, $H_{\text{SIA}}^f(p)$, of the $\langle 110 \rangle$, $\langle 111 \rangle$, and $\langle 100 \rangle$ SIA configurations are shown as a function of pressure in Fig. 3. Consistent with the monotonic decrease of E_{SIA}^f with volume in Fig. 2(a), H_{SIA}^f increases monotonically with pressure. Furthermore, similar with the volumetric

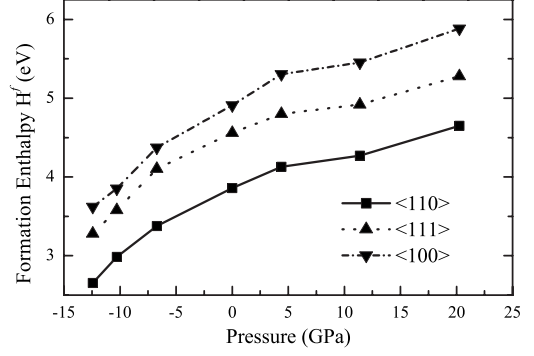


FIG. 3. Formation enthalpies $H_{\text{SIA}}^f(p)$ of the $\langle 110 \rangle$, $\langle 111 \rangle$, and $\langle 100 \rangle$ SIA configurations as a function of pressure.

strain behavior of E_{SIA}^f in Fig. 2(a), the pressure behavior of H_{SIA}^f s in Fig. 3 is nonlinear. Table III lists values of the SIA formation volume calculated from Eq. (8) under -7.0 and 14.9 GPa , respectively. Note that ΔV is smaller in the compression ($p > 0$) than in the expansion ($p < 0$) regime. The results indicate that under negative pressure, the SIA induces an expansion of the volume largely to compensate the change of pressure, thus dramatically releasing the elastic energy. On the other hand, under positive pressure, smaller changes of volume suffice to balance the external pressure, yielding a smaller accumulation of elastic energy. It should be emphasized that the trace of the formation volume tensor under constant pressure is not equal to that under constant volume, indicating the importance of atomic relaxation effects on electron densities and hence on defect formation energies.

B. Continuum elasticity and atomistic energetics of SIAs

For comparison, we present in Fig. 4 the results of formation energies of $\langle 110 \rangle$ and $\langle 111 \rangle$ SIAs under ε_v and ε_{33} deformations using continuum elasticity (CE) and molecular statics (MS) simulations.⁴³ The MS calculations employed the Ackland04 interatomic potential⁴⁴ for α -Fe. The supercell is $18 \times 18 \times 18 a_0^3$ containing 11 665 atoms with a SIA placed at the center. All atoms are allowed to relax at 0 K under the external deformation. The displacement field is then used to calculate the dipole tensor whose matrix elements are listed

TABLE III. Values of SIA formation volume, $\Delta V/\Omega_0$ for the $\langle 110 \rangle$, $\langle 111 \rangle$, and $\langle 100 \rangle$ SIA configurations under -7.0 , 14.9 , and 0.0 GPa . Here, Ω_0 is the equilibrium volume.

p (GPa)	$\Delta V/\Omega_0$		
	$\langle 110 \rangle$	$\langle 111 \rangle$	$\langle 100 \rangle$
-7.0	1.19	1.27	1.45
14.9	0.50	0.50	0.66
0.0	1.58	1.47 ^a 1.75 ^b	1.78 1.79 ^a

^aReference 45.

^bReference 46.

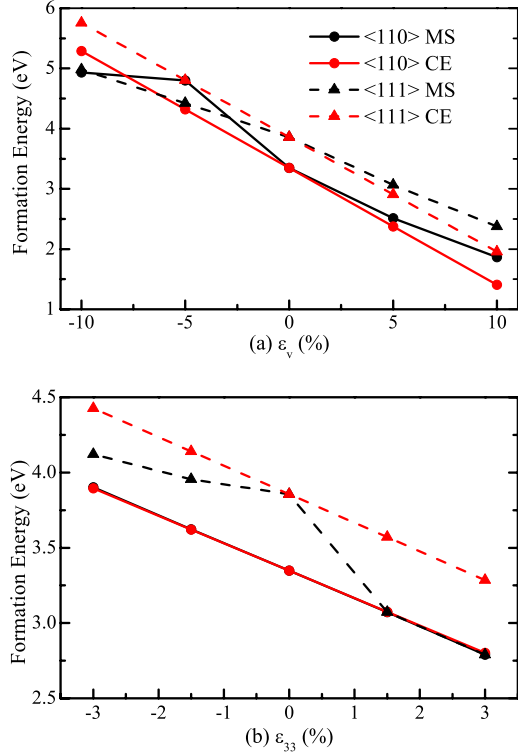


FIG. 4. (Color online) Formation energies of the $\langle 110 \rangle$ and $\langle 111 \rangle$ SIA configurations calculated by MS and CE under (a) volumetric ε_v and (b) uniaxial ε_{33} deformations. Black and red (gray) lines and symbols represent results of MS and CE, respectively.

in Table IV. Under $\varepsilon_v=0$, the MS approach gives $E_{\langle 110 \rangle}^f$ and $E_{\langle 111 \rangle}^f$ of 3.35 and 3.86 eV, respectively, which are consistent to the values reported by Terentyev *et al.*,¹¹ but lower than the DFT results. These values are also used as reference energies (with $E_{\text{int}}=0$ eV) for the CE calculations, also shown in Fig. 4.

As expected, the CE approach yields a linear dependence of the formation energy on both volumetric and uniaxial strains for the $\langle 110 \rangle$ and $\langle 111 \rangle$ SIAs in Figs. 4(a) and 4(b). Interestingly, the slopes of $E_{\langle 111 \rangle}^f$ and $E_{\langle 110 \rangle}^f$ with either ε_v or ε_{33} strain are parallel due to the fact that both $P_{33}^{(1)}$ s and $\sum P_{ii}^{(1)}$ (Table IV) for the $\langle 110 \rangle$ and $\langle 111 \rangle$ SIA are almost equal. Table IV also shows that the $\langle 111 \rangle$ SIA is equivalent under uniaxial deformation along the X , Y , and Z directions, while the $\langle 110 \rangle$ SIA is degenerate under ε_{11} and ε_{22} , but different

TABLE IV. Matrix elements of the dipole tensor \mathbf{P}^1 (in unit of eV) for the $\langle 110 \rangle$ and $\langle 111 \rangle$ SIAs.

	$P_{11}^{(1)}$	$P_{22}^{(1)}$	$P_{33}^{(1)}$	$P_{12}^{(1)}$	$P_{13}^{(1)}$	$P_{23}^{(1)}$
$\langle 110 \rangle$	20.02	20.02	18.22	-9.107	0.0	0.0
$\langle 111 \rangle$	19.01	19.01	19.01	-7.05	-7.05	7.05

under ε_{33} . These conclusions are consistent with our DFT results.

On the other hand, the MS simulations exhibit a nonlinear behavior of both $E_{\langle 110 \rangle}^f$ and $E_{\langle 111 \rangle}^f$ under ε_v and $E_{\langle 111 \rangle}^f$ under ε_{33} . Only $E_{\langle 110 \rangle}^f$ under ε_{33} shows perfect linearity. Detailed analysis indicates that this deviation arises from the atomic relaxation on and around the SIA, which strongly depends on the deformation of the system. It is important to note the difference between the results of MS and DFT due to the fact that empirical potentials cannot correctly describe the electronic structure and its response to deformation. This clearly indicates the important role of the electronic structure in determining the formation energy of SIA under deformation.

C. Analysis of *ab initio* energetics of SIAs

In order to elucidate the atomic origin of the orientation dependence of the formation energy under uniaxial deformation, we plot in Fig. 5 the atomic displacement fields (ADFs) of SIAs.^{17,47} The anisotropy of the ADF, which exhibits both compressive and tensile regions with respect to the external deformation, determines $E_{\text{SIA}}^f(\varepsilon_{ii})|_{i=1,2,3}$. The ADF of the $\langle 100 \rangle$ SIA on the $\{110\}$ plane, shown in Fig. 5(a), has a C_{2v} symmetry with all atoms dilating outward. The *largest* displacements along the $\langle 100 \rangle$ deformation direction are along (against) the uniaxial expansion (compression), thus leading to a decrease (increase) of the formation energy.

The ADF of the $\langle 110 \rangle$ SIA, shown in Fig. 5(b), has also a C_{2v} symmetry and is similar to that of the $\langle 100 \rangle$ SIA. Consequently, the strain behavior of $E_{\langle 110 \rangle}^f(\varepsilon)$ is similar to that of $E_{\langle 100 \rangle}^f(\varepsilon)$. The main difference is that for the $\langle 110 \rangle$ SIA, the *largest* dilation displacements of the ADF have components both parallel and perpendicular to the $\langle 100 \rangle$ deformation direction. Under uniaxial compression (expansion), the $[001]$ components increase (decrease) the elastic interaction, while the $\langle 110 \rangle$ components decrease (increase) the elastic interaction. The interplay of these two competing effects results in a

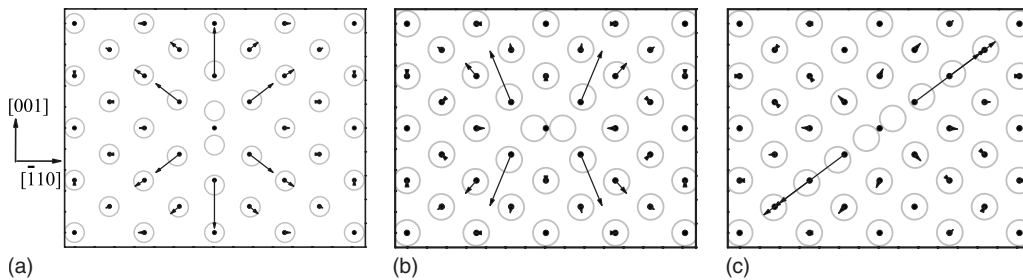


FIG. 5. Two-dimensional atomic displacement fields in the vicinity of a (a) $\langle 100 \rangle$, (b) $\langle 110 \rangle$, and (c) $\langle 111 \rangle$ SIAs on the $\{110\}$ plane. The small (large) solid (open) circles denote the perfect lattice (displaced) atomic positions. The lengths of the arrows are proportional to the atomic displacements.

TABLE V. Angle, θ , between the SIA axis and the $\langle 100 \rangle$ direction under uniaxial strains ε_{11} and ε_{33} .

ε_{11} (ε_{33}) (%)	Angle θ						
	-3.0	-2.0	-1.0	0.0	1.0	2.0	3.0
$\langle 110 \rangle$ (ε_{11})	47.1°	46.5°	45.6°	45.0°	44.2°	43.6°	42.9°
$\langle 110 \rangle$ (ε_{33})	90.0°	90.0°	90.0°	90.0°	90.0°	90.0°	90.0°
$\langle 111 \rangle$ (ε_{33})	58.0°	56.7°	55.6°	54.7°	54.0°	52.2°	30.8°
$\langle 100 \rangle$ (ε_{33})	0.0°	0.0°	0.0°	0.0°	0.0°	0.0°	0.0°

very weak dependence of the formation energy under uniaxial strain. For example, for the $\langle 110 \rangle$ SIA, the release of elastic interaction under uniaxial expansion results in lowering $E_{\langle 110 \rangle}^f(\varepsilon_{33} > 0)$, while under compressive strain, the two effects almost cancel out and $E_{\langle 110 \rangle}^f(\varepsilon_{33} < 0)$ is almost independent of strain. The ADF of the $\langle 111 \rangle$ SIA, shown in Fig. 5(c), has C_2 symmetry, with the *largest* atomic displacements along the $\langle 111 \rangle$ direction. Thus, the effect of uniaxial strain along $\langle 100 \rangle$ on the ADF is almost symmetric, yielding a symmetric variation of $E_{\langle 111 \rangle}^f$ with strain in Figs. 2(b) and 2(c).

The results of the ADF under uniaxial strain raise the interesting question whether the external macroscopic strain field can induce a rotation between different SIA orientations. For example, TEM experiments seem to suggest¹⁸ a reorientation of a SIA from $\langle 111 \rangle$ to $\langle 100 \rangle$. Thus, we have calculated the angle, θ , between the SIA axis and the deformation direction for the $\langle 110 \rangle$ (ε_{11}), $\langle 110 \rangle$ (ε_{33}), $\langle 111 \rangle$ (ε_{33}), and $\langle 100 \rangle$ (ε_{33}) SIA configurations under volumetric and uniaxial strain. We find that the volumetric deformation does not produce a rotation of the SIA and that under any ε_{ij} , the $\langle 110 \rangle$ (perpendicular to z axis), $\langle 110 \rangle$ (tilted with respect to z axis), $\langle 111 \rangle$, and $\langle 100 \rangle$ retain their zero-strain orientation, with $\theta=90.0^\circ$, 45.0° , 54.7° , and 0° , respectively. The corresponding values of θ as a function of uniaxial strain, ε_{33} , for the SIAs are listed in Table V. Interestingly, we find that for the $\langle 111 \rangle$ SIA under $\varepsilon_{33}=3\%$, there is a large reduction of θ from 54.7° to 30.8° , which remains saturated for larger uniaxial strains. This value of $\theta=30.8^\circ$ corresponds to a reorientation to a $\langle 11x \rangle|_{x=2.7}$ SIA. Thus, these results reveal an interesting SIA rotation mechanism induced by uniaxial deformation. Namely, uniaxial expansion facilitates the

$\langle 111 \rangle \rightarrow \langle 100 \rangle$ SIA reorientation through a transitional sessile $\langle 11x \rangle|_{x=2.7}$ SIA configuration, i.e., a $\langle 111 \rangle \rightarrow \langle 11x \rangle|_{x=2.7} \rightarrow \langle 100 \rangle$ SIA transformation. On the other hand, the $\langle 110 \rangle$ and $\langle 100 \rangle$ SIAs retain their original orientation under both uniaxial tension and compression. One should note that the stiffness of the $\langle 100 \rangle$ SIA indicates the irreversibility of the $\langle 111 \rangle \rightarrow \langle 100 \rangle$ transformation, consistent with previous atomistic simulations.¹⁹

We have also analyzed the differential charge density, defined as the difference between the total charge density of the system ρ and the superposition of isolated neutral atomic charge densities ρ_i^{atom} , placed at atomic sites

$$\rho^{\text{diff}}(\vec{r}) = \rho(\vec{r}) - \sum_i \rho_i^{\text{atom}}(\vec{r} - \vec{r}_i), \quad (9)$$

where \vec{r}_i is the position of the i th atom. Therefore, $\rho^{\text{diff}}(\vec{r})$ represents the net charge redistribution of the system.^{48,49} Figure 6 shows the differential charge density on the $\{110\}$ plane for the (a) $\langle 100 \rangle$, (b) $\langle 110 \rangle$, and (c) $\langle 111 \rangle$ SIAs under zero strain. For the $\langle 100 \rangle$ and $\langle 110 \rangle$ SIAs in panels (a) and (b), there is significant charge accumulation between the SIAs and their neighboring atoms along several different directions and exhibits a weak anisotropy of accumulating charge. As a result, these two SIAs retain their orientation under deformation, as shown in Table V, and do not show a preferential migration direction.^{6,18}

On the other hand, the $\langle 111 \rangle$ SIA in panel (c) shows an anisotropic one-dimensional directionality of accumulating charge, with substantial charge accumulation along $\langle 111 \rangle$ and minor accumulation along the perpendicular $\langle 112 \rangle$ direction. This anisotropy has two important consequences: First,

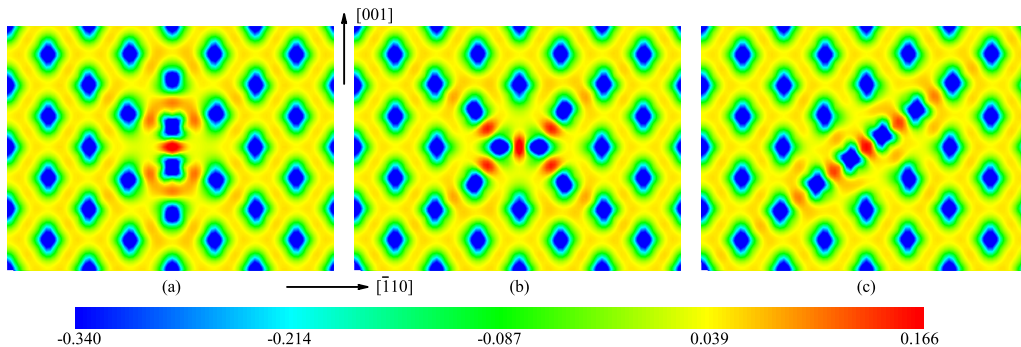


FIG. 6. (Color online) Differential charge density on the $\{110\}$ plane for the (a) $\langle 100 \rangle$, (b) $\langle 110 \rangle$, and (c) $\langle 111 \rangle$ SIAs under zero strain. Red (light gray) and blue (dark gray) contours represent electron accumulation and depletion, respectively. The contour interval is $2.5 \times 10^{-3} e/\text{\AA}^3$.

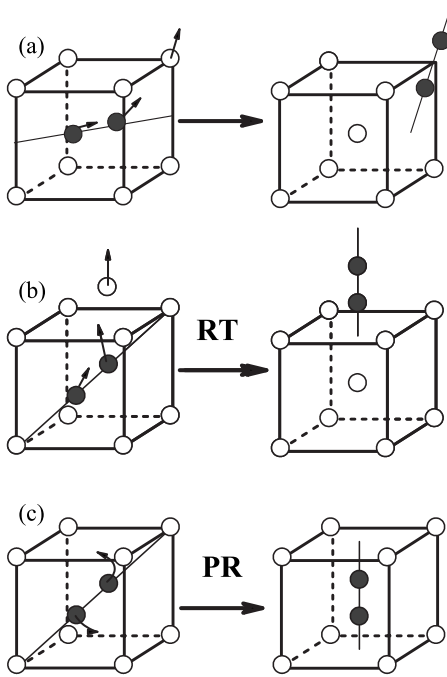


FIG. 7. Schematic representation of three migration paths between (a) $\langle 110 \rangle \{ 110 \}$ and $\langle 110 \rangle \{ 100 \}$ SIA, the $\langle 111 \rangle$ and $\langle 100 \rangle$ SIAs through (b) RT and (c) PR pathways, respectively.

the resistance to shearing along the $\langle 112 \rangle$ direction is weak. Hence, under the uniaxial strain ϵ_{33} , the component of the torque along the $\langle 112 \rangle$ is responsible for the reorientation of the SIA and the reduction of θ in Table V. Second, the $\langle 111 \rangle$ SIA prefers to migrate along the $\langle 111 \rangle$ direction because this type of one-dimensional motion does not involve the breaking of bonds, in agreement with previous atomistic simulations.^{19,50} Note another important asymmetry in ρ^{diff} of $\langle 111 \rangle$ SIA: there is stronger charge accumulation between the SIA pair and its clockwise neighboring atoms, giving rise to larger resistance of the SIA pair for clockwise rotation. This is consistent with the asymmetry found in Table V, where θ decreases by 23° under $\epsilon_{33}=3\%$ while it increases only by 4° under $\epsilon_{33}=-3\%$.

D. Migration of SIAs

In order to fully understand full evolution of SIA clusters under irradiation, one needs not only the information of the formation energies, but also the diffusion properties. In this section, we study the effect of external deformation on the preferred migration paths and associated activation energy barriers of the SIAs.

The study of all possible migration paths is out of reach for the present work. Therefore, we have focused on two specific transformations: under isotropic volumetric (ϵ_v) and uniaxial (ϵ_{33}) deformations. The first is between the two $\langle 110 \rangle$ SIAs and the second is between the $\langle 111 \rangle$ and $\langle 100 \rangle$ SIA configurations. Previous DFT calculations have identified the zero-strain lowest-energy barrier migration path for the $\langle 110 \rangle \leftrightarrow \langle 110 \rangle$ transformation shown in Fig. 7(a).⁶ However, the effect of volumetric or uniaxial strain on this trans-

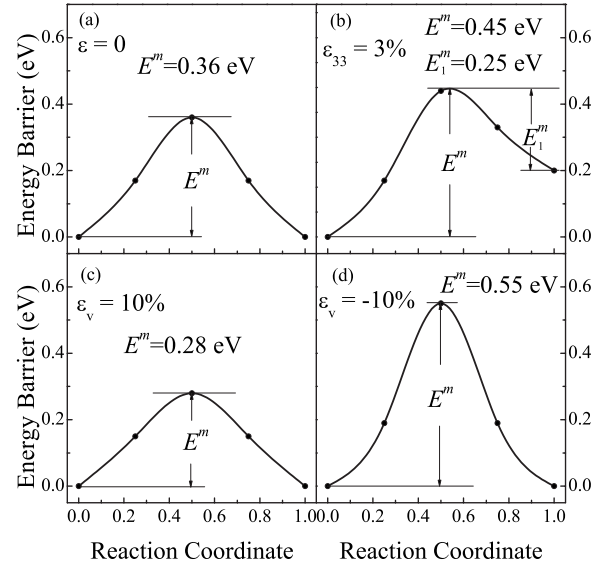


FIG. 8. Energy barrier along the $\langle 110 \rangle \{ 110 \} \leftrightarrow \langle 110 \rangle \{ 100 \}$ RT migration path under (a) zero strain, (b) uniaxial strain of $\epsilon_{33}=3\%$, and volumetric strains of (c) $\epsilon_v=10\%$ and (d) $\epsilon_v=-10\%$. The reaction coordinate refers to that of the dragged atom along the RT migration path.

formation remains an open question. Furthermore, the lowest-energy barrier migration path for the $\langle 111 \rangle \leftrightarrow \langle 100 \rangle$ SIA at zero or nonzero strain is not known. Thus, we have considered the effect of deformation on two possible migration paths: the pure on-site rotation (RT) and the rotation-translation (PR) path involving different sites shown in Figs. 7(b) and 7(c), respectively. The migration energy barrier, $E^m(\epsilon)$, is determined by employing the drag method,^{51,52} where the drag coordinate is chosen to be the straight-line interpolation between the initial and final state, with one of the SIA atoms fixed (dragged atom) and the remaining atoms relaxed. The reaction coordinate is a $3N$ -dimensional vector. For simplicity, the coordinate of the dragged atom which is renormalized to the total moving distance along a given migration path is referred to as the *reduced reaction coordinate*. In the following discussion, *reaction coordinate* is used for short.

The energy barrier along the $\langle 110 \rangle \{ 110 \} \leftrightarrow \langle 110 \rangle \{ 100 \}$ path is shown in Fig. 8 under (a) zero strain, (b) uniaxial strain of $\epsilon_{33}=3\%$, and volumetric strains of (c) $\epsilon_v=10\%$ and (d) $\epsilon_v=-10\%$. At zero strain, the migration barrier $E^m(\epsilon=0)$ is 0.36 eV and is in good agreement with the value of 0.34 eV of Fu *et al.*⁶ The $+10\%$ (-10%) volumetric expansion (compression) decreases (increases) E^m to 0.28 eV (0.55 eV). Since the diffusion reaction rate depends exponentially on E^m , these results show that the volumetric expansion (compression) can effectively enhance (suppress) the $\langle 110 \rangle \{ 110 \} \leftrightarrow \langle 110 \rangle \{ 100 \}$ transformation. One should also note that the volumetric deformation does not change the overall energy shape of the $\langle 110 \rangle \{ 110 \} \leftrightarrow \langle 110 \rangle \{ 100 \}$ migration path.

On the contrary, the uniaxial deformation with $\epsilon_{33}=3\%$ in Fig. 8(b) introduces an anisotropy in the energy barrier. Namely, migration barrier (E^m) for the $\langle 110 \rangle \{ 110 \} \rightarrow \langle 110 \rangle \{ 100 \}$ path increases to 0.45 eV while that

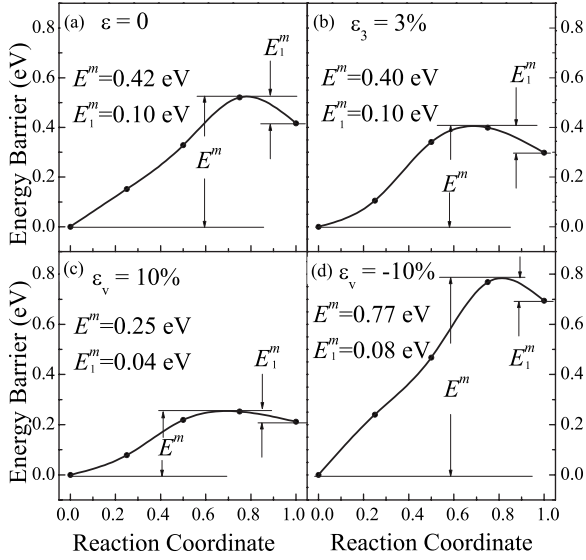


FIG. 9. Energy barrier along the $\langle 111 \rangle \leftrightarrow \langle 100 \rangle$ RT migration path under (a) zero strain, (b) uniaxial strain of $\varepsilon_{33}=3\%$, and volumetric strains of (c) $\varepsilon_v=10\%$ and (d) $\varepsilon_v=-10\%$. The reaction coordinate refers to that of the dragged atom along the RT migration path.

(E_1^m) for the reverse $\langle 110 \rangle \{100\} \leftarrow \langle 110 \rangle \{110\}$ path decreases to 0.25 eV. Consequently the uniaxial expansion lifts the degeneracy of the $\langle 110 \rangle$ SIA and renders the $\langle 110 \rangle \{110\}$ SIA orientation to be the ground state. Thus, we predict that under thermal equilibrium the majority of SIA clusters will occupy the $\langle 110 \rangle \{110\}$ configuration under $\varepsilon_{33} > 0$.

The energy barrier along the RT migration path is shown in Figs. 9 under (a) zero strain, (b) uniaxial strain $\varepsilon_{33}=3\%$, and volumetric strains of (c) $\varepsilon_v=10\%$ and (d) $\varepsilon_v=-10\%$. The volumetric expansion (compression) of $\varepsilon_v=10\%$ ($\varepsilon_v=-10\%$) decreases (increases) substantially the migration energy barrier, E^m , for the $\langle 111 \rangle \rightarrow \langle 100 \rangle$ RT to 0.25 eV (0.77 eV) from its zero-strain value of 0.42 eV. Interestingly, the volumetric strain reduces also the migration energy barrier, E_1^m , for the reverse $\langle 100 \rangle \rightarrow \langle 111 \rangle$ RT to 0.04 eV (0.08 eV) under $\varepsilon_v=10\%$ ($\varepsilon_v=-10\%$), compared to its zero-strain value of 0.1 eV. The reduction of both E^m and E_1^m under volumetric expansion increases exponentially the rate of the $\langle 100 \rangle \leftrightarrow \langle 111 \rangle$ RT and hence renders the diffusion process three dimensional. In contrast, the increase (decrease) of E^m (E_1^m) under volumetric compression decreases the rate of the $\langle 111 \rangle \rightarrow \langle 100 \rangle$ transformation, making thus the diffusion process one dimensional. On the other hand, the uniaxial expansion has a small effect on $\langle 111 \rangle \rightarrow \langle 100 \rangle$ RT path, where E_1^m decreases by 0.02 eV under $\varepsilon_{33}=3\%$.

The energy barrier along the $\langle 111 \rangle \leftrightarrow \langle 100 \rangle$ on-site PR migration path is shown in Fig. 10 under (a) zero strain, (b) uniaxial strain $\varepsilon_{33}=3\%$, and volumetric strains of (c) $\varepsilon_v=10\%$ and (d) $\varepsilon_v=-10\%$. The most striking feature of the energy profile under zero strain is the appearance of a global minimum between the $\langle 111 \rangle$ and $\langle 100 \rangle$ orientations, corresponding to the $\langle 11x \rangle|_{x=2,7}$ dumbbell, which is also the ground state under the uniaxial strain of $\varepsilon_{33}=3\%$ in panel (b). The zero-strain migration energy barriers for the $\langle 11x \rangle|_{x=2,7} \rightarrow \langle 100 \rangle$ and the $\langle 111 \rangle \rightarrow \langle 11x \rangle|_{x=2,7}$ transformation

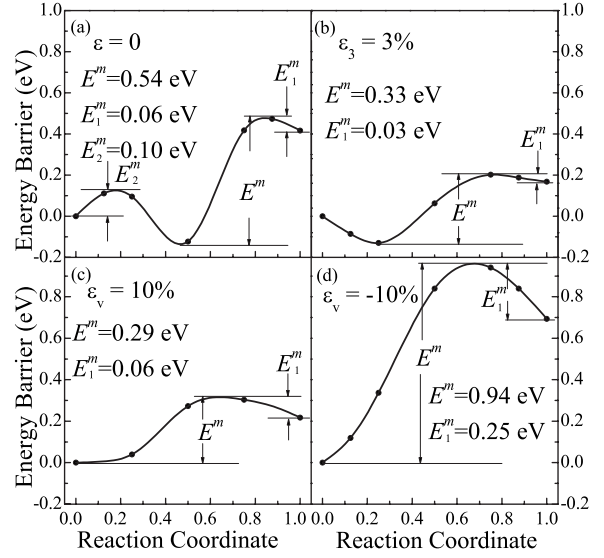


FIG. 10. Energy barrier along the $\langle 111 \rangle \leftrightarrow \langle 100 \rangle$ on-site PR migration path under (a) zero strain, (b) uniaxial strain of $\varepsilon_{33}=3\%$, and volumetric strains of (c) $\varepsilon_v=10\%$ and (d) $\varepsilon_v=-10\%$. The reaction coordinate refers to that of the dragged atom along the PR migration path.

paths are 0.54 and 0.10 eV, respectively. The external volumetric and uniaxial deformations have a dramatic effect on the PR migration energy profile. The volumetric deformation removes the global energy minimum and the expansion (compression) of $\varepsilon_v=10\%$ ($\varepsilon_v=-10\%$) decreases (increases) substantially the migration energy barrier, E^m , for the $\langle 111 \rangle \rightarrow \langle 100 \rangle$ PR to 0.29 eV (0.94 eV) from its zero-strain value of 0.54 eV. Note that the migration energy barrier for the reverse $\langle 100 \rangle \rightarrow \langle 111 \rangle$ PR path does not change under the volumetric expansion of $\varepsilon_v=10\%$, whereas it increases to the value of 0.25 eV under $\varepsilon_v=-10\%$. Thus, volumetric expansion (compression) enhances (suppresses) the $\langle 111 \rangle \rightarrow \langle 100 \rangle$ on-site rotation.

It is interesting to note that the uniaxial strain in Fig. 10(b) removes the migration energy barrier E_2^m for the $\langle 111 \rangle \rightarrow \langle 11x \rangle|_{x=2,7}$ transformation and decreases the energy barrier for the $\langle 11x \rangle|_{x=2,7} \rightarrow \langle 100 \rangle$ transition to the value of 0.33 eV. Thus, the uniaxial strain renders the $\langle 111 \rangle$ SIA unstable and the $\langle 11x \rangle|_{x=2,7}$ SIA be the metastable configuration. This result explains the spontaneous reorientation of the $\langle 111 \rangle$ SIA discussed in Sec. III A. Note that the uniaxial strain reduces the energy barrier of E_1^m to 0.03 eV and facilitates the reverse $\langle 100 \rangle \rightarrow \langle 11x \rangle|_{x=2,7}$ transformation, thus stabilizing the $\langle 11x \rangle|_{x=2,7}$ orientation. Comparison of the energy profiles in Figs. 9 and 10 shows that in general the diffusion barrier for the RT pathway is lower, except under $\varepsilon_{33} > 0$. This suggests that with the exception of uniaxial expansion, the RT is the preferential path for $\langle 111 \rangle \rightarrow \langle 100 \rangle$.

As pointed out by Dederichs and Schroeder²⁷ and Aziz,³⁸ the effects of strain on diffusion can be described quantitatively by CE theory. More specifically, the diffusion coefficient $D(p)$ under volumetric deformation can be written as

$$D(p) = D(p=0) \exp\left(\frac{-p(\Delta V + V^m)}{kT}\right), \quad (10)$$

where ΔV is the formation volume defined in Eq. (8) and V^m is the migration volume which is the additional volume change at the saddle point. As shown in Table III, ΔV is positive for all the three SIA configurations and V^m is also positive for all the three paths.⁵³ Thus, CE predicts that the volumetric expansion ($p > 0$) [compression ($p < 0$)] decreases (increases) $D(p)$ which corresponds to an increase (decrease) of the energy barrier E^m , consistent with our *ab initio* results. On the other hand, the uniaxial deformation breaks the cubic symmetry, thus yielding different rate of migration paths along different crystallographic directions.²⁷ This conclusion of CE theory is consistent with our atomistic DFT results shown in Fig. 8(b) which clearly show the asymmetry of transformation between the $\langle 110 \rangle$ SIAs with different orientations.

IV. CONCLUSIONS

In conclusion, we have employed *ab initio* electronic structure calculations to study the effects of external deformation on the stability and mobility of SIAs in α -Fe. The *ab initio* results demonstrate that the volumetric and uniaxial strain dependences of the SIA formation energy are different in the expansion and compression regimes, in contrast to the linear behavior in continuum elasticity theory. The calculations reveal that the uniaxial strain induces an interesting SIA reorientation, which proceeds via the $\langle 111 \rangle \rightarrow \langle 11x \rangle|_{x=2.7}$ transformation. The differential charge density is more isotropic for the $\langle 110 \rangle$ and $\langle 100 \rangle$ configurations, while it exhibits a one-dimensional directionality for the $\langle 111 \rangle$ SIA, which is responsible for its higher reorientation propensity under uniaxial deformation. We have also calculated the effect of strain on the formation energies using MS and CE approaches. Comparison of the results from DFT to those of MS and CE indicates the importance of electronic structure in determining the formation energy of point defects under deformation.

We have also studied the effect of external deformation on the migration paths and associated activation energy barriers

for the $\langle 110 \rangle \{110\} \leftrightarrow \langle 110 \rangle \{100\}$ and $\langle 111 \rangle \rightarrow \langle 100 \rangle$ transformations. For the first transformation, the volumetric expansion (compression) decreases (increases) the migration energy barrier, while the uniaxial expansion ϵ_{33} lifts the degeneracy of the $\langle 110 \rangle$ SIA and renders the $\langle 110 \rangle \{110\}$ SIA orientation to be the ground state. For the second transformation, the RT migration is found to be the preferential path. The volumetric expansion (compression) decreases (increases) substantially the migration energy barrier for the $\langle 111 \rangle \rightarrow \langle 100 \rangle$ transformation. The volumetric deformation decreases also the migration barrier for the reverse $\langle 100 \rangle \rightarrow \langle 111 \rangle$ transformation. The interplay between these two activation barriers under volumetric deformation renders the diffusion process three (one) dimensional under volumetric expansion (compression). The volumetric and uniaxial deformations have a dramatic effect also on the PR migration energy profile. The volumetric deformation removes the global energy minimum corresponding to the $\langle 11x \rangle|_{x=2.7}$ dumbbell. The expansion (compression) decreases (increases) substantially the migration energy barrier for the $\langle 111 \rangle \rightarrow \langle 100 \rangle$ on-site PR. The uniaxial strain removes (decreases) the migration energy barrier for the $\langle 111 \rangle \rightarrow \langle 11x \rangle|_{x=2.7} (\langle 11x \rangle|_{x=2.7} \rightarrow \langle 100 \rangle)$ transformation, leading to the spontaneous reorientation of the $\langle 111 \rangle$ SIA. The *ab initio* results of the effect of strain on the migration energy are in agreement with CE theory and indicate that the external strain field is a key factor to modulate the orientation of mono-SIA in α -Fe. These calculations demonstrate that changes in the electronic structure induced by global elastic deformation lead to additional contributions to the formation and migration energies, which cannot be adequately accounted for neither by elasticity theory nor by empirical interatomic potentials.

ACKNOWLEDGMENTS

The authors thank A. Ramasubramaniam for his insightful help. This research was supported by NSF-NIRT Grant No. CMS-0506841, NSF-PREM Grant No. DMR-00116566, DOE NERI Grant No. DE-FC07-06ID14748, and Office of Fusion Energy through Grant No. DE-FG02-03ER54708 with UCLA.

¹T. Diaz de la Rubia, H. M. Zbib, T. A. Khraishi, B. D. Wirth, M. Victoria, and M. J. Caturla, *Nature (London)* **406**, 871 (2000).
²B. L. Eyre and A. F. Bartlett, *Philos. Mag.* **12**, 261 (1965).
³B. L. Eyre and A. F. Bartlett, *J. Nucl. Mater.* **47**, 143 (1973).
⁴M. T. Robinson, *J. Nucl. Mater.* **216**, 1 (1994).
⁵C. Domain and C. S. Becquart, *Phys. Rev. B* **65**, 024103 (2001).
⁶C. C. Fu, F. Willaime, and P. Ordejón, *Phys. Rev. Lett.* **92**, 175503 (2004).
⁷D. A. Terentyev, T. P. C. Klaver, P. Olsson, M.-C. Marinica, F. Willaime, C. Domain, and L. Malerba, *Phys. Rev. Lett.* **100**, 145503 (2008).
⁸J. Marian, B. D. Wirth, A. Caro, B. Sadigh, G. R. Odette, J. M. Perlado, and T. Diaz de la Rubia, *Phys. Rev. B* **65**, 144102

(2002).

⁹Yu. N. Osetsky, A. Serra, and V. Priego, *J. Nucl. Mater.* **276**, 202 (2000).
¹⁰B. D. Wirth, G. R. Odette, D. Maroudas, and G. E. Lucas, *J. Nucl. Mater.* **276**, 33 (2000).
¹¹D. A. Terentyev, L. Malerba, and M. Hou, *Phys. Rev. B* **75**, 104108 (2007).
¹²P. Ehrhart, K. H. Robrock, and H. R. Schober, in *Physics of Radiation Effects in Crystals*, edited by R. A. Johnson and A. N. Orlov (Elsevier, Amsterdam, 1986), p. 63.
¹³G. J. Ackland, D. J. Bacon, A. F. Calder, and T. Harry, *Philos. Mag. A* **75**, 713 (1997).
¹⁴B. J. Lee, M. I. Baskes, H. Kim, and Y. K. Cho, *Phys. Rev. B* **64**,

- 184102 (2001).
- ¹⁵F. Willaime, C. C. Fu, M. C. Marinica, and J. Dalla Torre, Nucl. Instrum. Methods Phys. Res. B **228**, 92 (2005).
- ¹⁶V. Gavini, Phys. Rev. Lett. **101**, 205503 (2008).
- ¹⁷J. Marian, B. D. Wirth, J. M. Perlado, G. R. Odette, and T. Diaz de la Rubia, Phys. Rev. B **64**, 094303 (2001).
- ¹⁸K. Arakawa, M. Hatanaka, E. Kuramoto, K. Ono, and H. Mori, Phys. Rev. Lett. **96**, 125506 (2006).
- ¹⁹J. Marian, B. D. Wirth, and J. M. Perlado, Phys. Rev. Lett. **88**, 255507 (2002).
- ²⁰W. G. Wolfer and M. Ashkin, Scr. Metall. Mater. **7**, 1175 (1973).
- ²¹E. J. Savino, Philos. Mag. **36**, 323 (1977).
- ²²C. N. Tomé, H. A. Cecatto, and E. J. Savino, Phys. Rev. B **25**, 7428 (1982); E. J. Savino and C. N. Tomé, J. Nucl. Mater. **108-109**, 405 (1982).
- ²³C. H. Woo, J. Nucl. Mater. **120**, 55 (1984).
- ²⁴M. J. Chen and Y. M. Sheu, Appl. Phys. Lett. **89**, 161908 (2006).
- ²⁵M. J. Aziz, Y. Zhao, Hans-J. Gossmann, S. Mitha, S. P. Smith, and D. Schiferl, Phys. Rev. B **73**, 054101 (2006).
- ²⁶C. P. Flynn, *Point Defects and Diffusion* (Clarendon Oxford, London, 1972).
- ²⁷P. H. Dederichs and K. Schroeder, Phys. Rev. B **17**, 2524 (1978).
- ²⁸G. Kresse and J. Hafner, Phys. Rev. B **47**, 558(R) (1993).
- ²⁹G. Kresse and J. Furthmüller, Phys. Rev. B **54**, 11169 (1996).
- ³⁰J. P. Perdew, K. Burke, and M. Ernzerhof, Phys. Rev. Lett. **80**, 891 (1998).
- ³¹P. E. Blöchl, Phys. Rev. B **50**, 17953 (1994).
- ³²H. J. Monkhorst and J. D. Pack, Phys. Rev. B **13**, 5188 (1976).
- ³³D. Iotova, N. Kioussis, and S. P. Lim, Phys. Rev. B **54**, 14413 (1996).
- ³⁴M. J. Gillan, J. Phys.: Condens. Matter **1**, 689 (1989).
- ³⁵A. Ramasubramaniam (private communication).
- ³⁶R. Siems, Phys. Status Solidi **30**, 645 (1968).
- ³⁷C. Teodosiu, *Elastic Models of Crystal Defects* (Springer-Verlag, New York, 1982).
- ³⁸M. J. Aziz, Appl. Phys. Lett. **70**, 2810 (1997).
- ³⁹M. S. Daw, W. Windl, and M. Laudon, in *Proceedings of the International Conference on Computational Nanoscience and Nanotechnology*, edited by M. Laudon and B. Romanowicz (Computational Publications, Boston, 2001), p. 96.
- ⁴⁰G. Ho, M. Ong, K. Caspersen, and E. Carter, Phys. Chem. Chem. Phys. **9**, 4951 (2007).
- ⁴¹S. Mukherjee, R. Cohen, and O. Gülseren, J. Phys.: Condens. Matter **15**, 855 (2003).
- ⁴²C. Kittel, *Introduction to Solid State Physics*, 6th ed. (Wiley, New York, 1987).
- ⁴³We did not show results of $\langle 100 \rangle$ SIA because using Ackland04 potential (Ref. 44) $\langle 100 \rangle$ becomes unstable and rotates to $\langle 110 \rangle$.
- ⁴⁴G. J. Ackland, M. I. Mendelev, D. J. Srolovitz, S. Han, and A. V. Barashev, J. Phys.: Condens. Matter **16**, S2629 (2004).
- ⁴⁵R. E. Stoller, G. R. Odette, and B. D. Wirth, J. Nucl. Mater. **251**, 49 (1997).
- ⁴⁶B. J. Lee, B. D. Wirth, J. H. Shim, J. Kwon, S. C. Kwon, and J. H. Hong, Phys. Rev. B **71**, 184205 (2005).
- ⁴⁷S. Han, L. A. Zepeda-Ruiz, G. J. Ackland, R. Car and D. J. Srolovitz, Phys. Rev. B **66**, 220101(R) (2002).
- ⁴⁸S. N. Sun, N. Kioussis, S. P. Lim, A. Gonis, and W. H. Gourdin, Phys. Rev. B **52**, 14421 (1995).
- ⁴⁹Z. Z. Chen and C. Y. Wang, Phys. Rev. B **72**, 104101 (2005).
- ⁵⁰B. D. Wirth, G. R. Odette, D. Maroudas, and G. E. Lucas, J. Nucl. Mater. **244**, 185 (1997).
- ⁵¹G. Henkelman, G. Jóhannesson, and H. Jónsson, in *Theoretical Methods in Condensed Phase Chemistry*, edited by S. D. Schwartz (Springer-Verlag, Berlin, 2002), p. 272.
- ⁵²J. C. Hamilton and S. M. Foiles, Phys. Rev. B **65**, 064104 (2002).
- ⁵³The migration volume is $V^m = V_s - V_0$, where V_0 is the initial-state volume of a cube of edge length $L = 2a_0$ centered at the midpoint of the SIA with eight atoms at the apices and V_s is the corresponding volume at the saddle point. In the absence of external deformation, V^m is (a) 1.3 \AA^3 , (b) 2.1 \AA^3 , and (c) 0.4 \AA^3 , respectively, of the migration paths shown in Fig. 7.